Pre-print of a published manuscript

Evaluation of enhanced nucleate boiling performance through wall-temperature distributions on PDMS-silica coated and non-coated laser textured stainless steel surfaces

Matevž Zupančič, MaticMože, PeterGregorčič, AnžeSitar, IztokGolobič

DOI: https://doi.org/10.1016/j.ijheatmasstransfer.2017.03.128
Published in: International Journal of Heat and Mass Transfer, Volume 111, August 2017, Pages 419-428

Received: 16 February 2017
Accepted: 23 March 2017

Evaluation of enhanced nucleate boiling performance through wall-temperature distributions on PDMS-silica coated and non-coated laser textured stainless steel surfaces

Matevž Zupančič*, Matic Može, Peter Gregorčič, Anže Sitar, Iztok Golobič

Faculty of Mechanical Engineering, University of Ljubljana, Aškerčeva 6, 1000 Ljubljana, Slovenia

*matevz.zupancic@fs.uni-lj.si, +386 1 477 1 309

Abstract

Nucleate boiling was examined on Joule heated stainless steel foils, functionalized by PDMS-silica coating and/or nanosecond-laser texturing. The nucleating bubbles and transient temperature fields were visualized through high-speed IR and video recordings. The differences in boiling performance were evaluated through wall-temperature distributions. Results confirmed that smooth surfaces require high activation temperatures and produce larger bubbles, while wall-temperature distributions display higher standard deviations, higher local superheats, and bimodal shapes. Similarly, relatively high activation temperatures were observed on the superhydrophilic surface, where the enhanced liquid replenishment on the active nucleation sites reduces the bubble departure diameters and prevents formation of local hotspots. Consequently, the analyzed temperature distributions have negative skewness and decreased standard deviation. The highest heat transfer coefficient was achieved on a laser textured surface with non-uniform wettability and multi-scale microcavities. Here, nucleation site density was as high as 200 cm^{-2} at 300 kW/m^2, while wall-temperature distributions demonstrated by far the lowest standard deviation. The temperature distributions also proved that annealed PDMS-silica coating significantly increased the thermal resistance of the entire heater. On the contrary, laser textured surfaces provided an even better boiling performance compared to coated surfaces and did not increase heater's thermal resistance. This additionally endorses the coating-free, direct laser texturing method as a cutting-edge technology in the development of surfaces capable of significantly enhanced boiling heat transfer.

Keywords: enhanced boiling heat transfer; high-speed IR thermography; wall-temperature distributions; PDMS-silica coating; nanosecond laser texturing

1 Introduction

Phase change heat transfer allows for the dissipation of high heat fluxes and provides very high heat transfer coefficients and is consequently indispensable in many heat transfer applications. Especially nucleate boiling has an important role in cooling of microelectronics, supercomputers, and nuclear power plant fuel rods [1–4]. Due to constant advancements in the aforementioned fields, perpetual enhancements of boiling heat transfer are also required.

In pool boiling, a seemingly infinite and stationary amount of boiling liquid is considered. One of the pool boiling regimes is nucleate boiling, during which the liquid is vaporized and leaves the heating surface in the form of vapor bubbles of various sizes. This boiling regime is characterized by a relatively low surface superheat, i.e. the difference between the temperature of the surface and the saturation temperature of the surrounding liquid. Additionally, high heat fluxes can be removed from the surface and high heat transfer coefficients are obtainable. Therefore, it is the most prudent regime for the majority of boiling heat transfer applications. As both the boiling process and the accompanying heat transfer can be significantly influenced through the modification of the heating surface and its interaction with the liquid [5–8], the desire to enhance both antecedent crucial pool boiling factors lead to the development of various surface modification techniques [9–12].

In recent years, laser texturing is gaining popularity as a surface modification approach for the fabrication of surfaces capable of enhanced boiling heat transfer due to its many advantages compared to most other methods. Laser texturing is relatively fast and flexible; furthermore, laser textured surfaces are quite durable and the production generally does not involve any coatings or chemicals thus reducing or eliminating the thermal resistance of the modified surfaces and - at the same time - making the method more environmentally acceptable. Both the wettability and the micro/nanostructure of surfaces can be modified using laser texturing [13–16]. Both parameters greatly influence boiling heat transfer and are frequently closely intertwined; in many cases changing the micro/nanostructure causes the wettability of the surface to change and vice versa. Through careful manipulation and combination of both parameters, especially by means of laser surface texturing, considerable enhancements of boiling heat transfer can be achieved [17,18].

Several different approaches are possible when it comes to analyzing the boiling heat transfer performance of various surfaces. The most common mean of analysis is the so-called boiling curve, which defines the relation between the surface superheat and the heat flux [19]. A significant advantage of this approach is the fact that the experimental data needed to plot a boiling curve is easily obtained. However, a major drawback of the boiling curve is temporal and spatial averaging; in other words, local features of the boiling phenomena [20–22] are completely disregarded. Therefore, the boiling process is not characterized in its entirety. As we have previously shown [23], the evaluation of the boiling process based on wall-temperature distributions grants a significantly better insight into the phenomena during boiling on a particular surface. However, the prerequisite for the calculation of the distributions is an abundant amount of data regarding the transient temperature fields on the boiling surface, which requires a rather specific approach to the temperature measurement. The distributions show not

only the minimum, maximum, and mean temperatures, but also the standard deviation and the overall shape of wall-temperature distribution. This allows for a better understanding of the boiling performance of each individual surface as high local superheats and large standard deviations of the surface temperature are most undesired due to the possibility of the onset of a boiling crisis [24] as well as the additional thermal stress and fatigue as a result of locally concentrated thermal loads [25].

In this study, we present an in-depth analysis of enhanced pool boiling performance on several recently developed coated and non-coated surfaces with an emphasis on the comparison of spatiotemporal temperature fields during boiling. Stainless steel foil with a thickness of 25 μm was used as the base material and high-speed IR thermography was employed to record unsteady temperature fields on the foil. Manufacturing procedures and nucleate boiling curves for these surfaces were already shown in our previous studies [12,18]. Here, we aim to exploit the concept of wall-temperature distributions [23] and show the important differences in the boiling performance of various surfaces, which cannot be observed solely on the basis of the boiling curves.

2 Experiments and Methods

2.1 Pool boiling experiments

The schematic representation of the pool boiling experimental setup is shown in Fig. 1. As the experimental setup has been described in details in our previous publications [12,18], we are hereby providing only a brief overview of its vital components. The setup consisted of a double glazed glass boiling chamber with external dimensions of 170×100×100 mm^3 mounted between two steel plates. The 25 μm thick stainless steel (AISI 316) foil with an effective heat transfer area of 17×27 mm^2 was affixed to the electrical contacts and the whole assembly was inserted into the boiling chamber. The foil acted as a heater by the Joule heat generation principle. Its bottom side was covered with a thin layer of a high emissivity paint, which enabled us to use a high-speed IR camera for transient temperature measurements. In order to avoid placing the camera directly under the fluid-filled boiling chamber, a golden mirror at an angle of 45° was used to reflect IR radiation towards the IR camera. Double-distilled water was used as the working fluid and was degassed through a two-hour session of vigorous boiling prior to every series of measurements using a cartridge heater. This heater was also used to maintain the saturated state of the liquid and was turned off momentarily during every measurement in order to prevent it from influencing the heat transfer from the foil and therefore affecting the experimental results.

The heat generation was determined on the basis of the voltage drop across the foil and the supplied electrical current measured through the voltage drop on a reference resistor. To obtain the heat flux, the calculated heat generation was divided by the effective heat transfer area of the foil. Uniform heat flux was assumed across the entire surface.

Visible spectrum high-speed camera Casio Exilim EX-F1 recording at 1200 fps was used for the visualization of the bubble formation and departure dynamics. A high-speed IR camera FLIR SC6000 recording at 1000 fps with the resolution of 250 μm per pixel was employed for the unsteady temperature field measurements. The average wall temperature was calculated by temporal and spatial averaging of the temperature fields during a 10 s IR camera recording (corresponding to 10,000 frames). The expanded absolute measurement uncertainty of the temperature was determined to be 2.0 K, the expanded relative measurement uncertainty of the heat flux was 0.5 % and the maximum expanded measurement uncertainty of the heat transfer coefficient was calculated as 3.4 kW/m^2K.

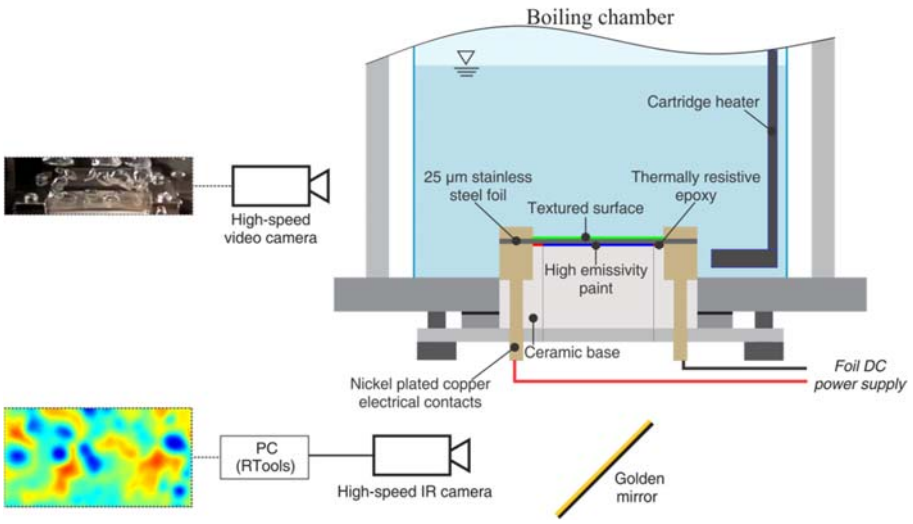

Fig. 1: Pool boiling experimental setup.

2.2 Manufacturing of functionalized surfaces

Several different methods were utilized to functionalize surfaces for enhanced boiling heat transfer including hydrophobic coating application, laser heat treatment of the said coating, and direct laser texturing of the surfaces. All manufacturing procedures, surface characterization and analysis, and nucleate boiling curves are explained in detail in our previous studies [12,18]. Table 1 lists all of the surfaces used in this study, while Fig. 2 shows SEM and AFM images and nucleate boiling curves obtained during saturated pool boiling experiments [12,18]. Stainless steel was used as the base material in all cases due to its favorable resistance to corrosion, widespread use in thermal and process engineering, and because previous research indicates the possibility of changing its wettability by means laser texturing [15,16].

The first group of surfaces [Fig. 2(b)] was created by applying polydimethylsiloxane (PDMS) coated fumed silica to the 25-μm-thick stainless steel substrate rendering the surfaces highly hydrophobic. The water contact angle on the hydrophobic coating was 138°. It was shown [12] that thermal treatment of the coating caused oxidation of non-polar methyl groups as well as formation of silicon oxide and silicon carbide, which resulted in a wettability transition from hydrophobic to superhydrophilic. Based on this, we developed an annealed superhydrophilic surface (sample SHPI) and a laser treated biphilic surface (sample $BPI_{0.25}$). A pulsed nanosecond Nd:YAG laser (wavelength of 1064 nm and pulse duration of 340 ns) was used to locally heat the coating and consequently modify (increase) the wettability of the surface. Biphilic surfaces, i.e. surfaces with intermittent regions of significantly different wettabilities, are known to provide significant boiling heat transfer improvements [11,23,26,27].

The second group of surfaces [e.g. see Fig. 2(c)] consisted of surfaces, textured using solely a marking nanosecond Nd:YAG laser (wavelength of 1064 nm and pulse duration of 40 ns). The laser textured surfaces produced on 25-μm-thick S316 stainless steel foils were either slightly hydrophilic (samples F1 and F2), superhydrophilic (sample F3) or had non-uniform wettability (sample F4) immediately after texturing. Temporal changes of the wettability were also

investigated; the wettability decreased slightly over time [18], which is consistent with the results of other researchers [15,16]. In addition to non-uniform wettability of the surface F4, this sample included multi-scale microcavities on specific regions based on local laser texturing parameters. An in-depth description of the laser texturing and a complete characterization of the modified surfaces can be found elsewhere [18].

Table 1: List of surfaces used in pool boiling experiments.

Label	Description	Static water contact angle (°)	Modification technique	Modification parameters
SS	25-s-thick S316 stainless steel foil (reference).	88	None.	/
SHPI	Surface with annealed coating (superhydrophilic).	< 1	PDMS-silica coating + annealing.	Annealed at 600 °C for 8 h.
$BPI_{0.25}$	Biphilic surface (superhydrophilic / hydrophobic).	< 1 / 138	PDMS-silica coating + local laser heat treatment of the coating.	0.25×0.25 mm^2 hydrophobic spot size, 1.5 mm pitch between spots.
F1	Laser-textured surface (hydrophilic).	64	Direct Nd:YAG laser texturing.	4.0 J/cm^2 laser pulse fluence, grid texturing pattern.
F2	Laser-textured surface (hydrophilic).	66	Direct Nd:YAG laser texturing.	4.0 J/cm^2 laser pulse fluence, completely textured.
F3	Laser-textured surface (superhydrophilic).	< 1	Direct Nd:YAG laser texturing.	6.0 J/cm^2 laser pulse fluence, completely textured.
F4	Laser-textured surface (non-uniform wettability, microcavities, microporous).	non-uniform	Direct Nd:YAG laser texturing.	9.0 J/cm^2 laser pulse fluence, non-uniform grid texturing pattern

Surfaces were tested in various heat flux ranges but only the results for the 0-400 kW/m^2 range are shown in Fig. 2(d). The reference surface SS and the laser-textured surface F1 were not able to dissipate heat fluxes above 300 kW/m^2 without the onset of the CHF conditions and data is therefore shown only for the measurable range for these two surfaces. It is important to note that the CHF value, obtained on a thin substrate, is not comparable with the CHF calculated from Zuber's theoretical model [28], which considers only hydrodynamic effects while ignoring heat transfer at the heated surface, thermal properties, and thickness of the surface [5]. Therefore, the maximum values of the heat flux in Fig. 2 do not necessarily represent the CHFs for tested surfaces.

Judging from the boiling curves, all surfaces with the exception of the surface F1 show boiling heat transfer enhancements as the superheats are lower at a given heat flux compared to the reference SS surface. The greatest improvement was provided by the biphilic surface $BPI_{0.25}$ and the laser-textured surface F4. While the surfaces F2, F3, and SHPI provided an enhancement over the reference surface, they were considerably outperformed by the other aforementioned surfaces.

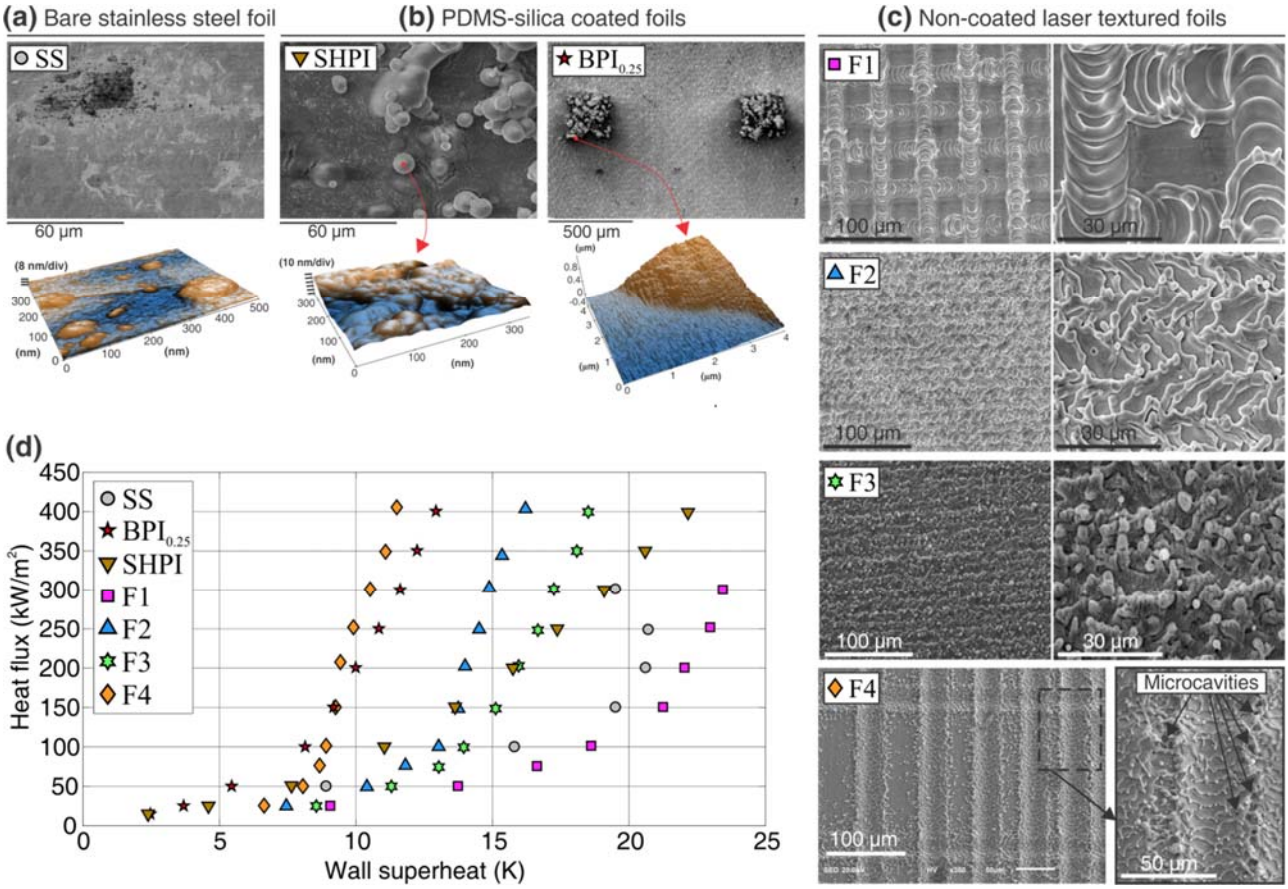

Fig 2: SEM and AFM images of (a) bare stainless steel foil[12], (b) superhydrophilic and biphilic PDMS-silica coated foils [12], (c) non-coated laser textured foils [18] and (d) nucleate pool boiling curves in the range up to 400 kW/m^2.

3 Results and Discussion

3.1 High-speed visualization

Representative images showing nucleate boiling at 25 kW/m^2 and 100 kW/m^2 were extracted from the high-speed camera recordings and are shown in Fig 3(a). The recordings obtained at 100 kW/m^2 were further analyzed and the average bubble departure diameters were measured with the results provided in Fig. 3(b). At 25 kW/m^2, the nucleate boiling regime has not yet been fully established on surfaces SS, F1, F2, and F3. Therefore, laser textured samples F1-F3 provided no enhancement regarding the onset of nucleate boiling (ONB), i.e. moving the ONB towards lower surface superheats. Nonetheless, the average bubble departure diameter at 100 kW/m^2 was approximately 20% lower on surfaces F1 and F2 and 50% lower on the surface F3.

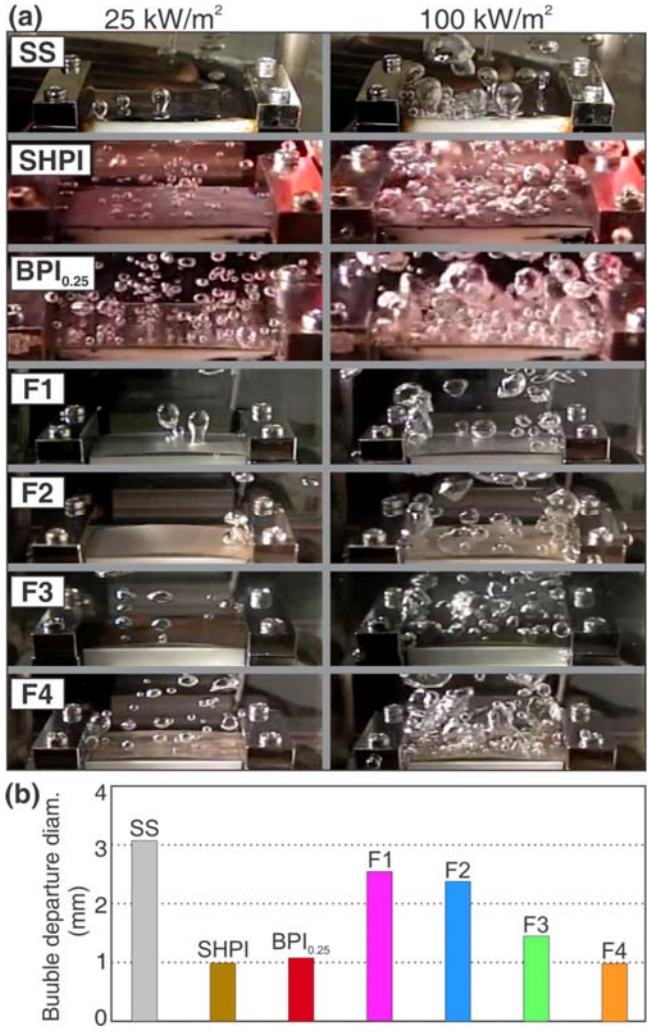

Fig 3: (a) Sample video images of nucleate boiling on all tested samples at 25 kW/m^2 and 100 kW/m^2,and (b) average bubble departure diameters at 100 kW/m^2.

The lowest temperature of the ONB was achieved on the biphilic sample $BPI_{0.25}$, which consequently resulted in the highest heat transfer coefficient at the early stages of the nucleate boiling regime [e.g. see Fig 2(d)]. High-speed video confirmed that this sample provided the highest nucleation site density at 25 kW/m^2 since each hydrophobic spot represented an active nucleation site. In Fig. 3(a), enhanced boiling activity on surfaces SHPI, $BPI_{0.25}$, and F4 compared to the other samples is clearly noticeable. All of these surfaces provided much higher active nucleation site densities and up to 70% smaller bubble departure diameters compared to the SS sample (the reference surface). At heat fluxes above 100 kW/m^2, the emerging vapor bubbles prevent visual observation of the boiling surface and high-speed IR thermography becomes the main mean of analysis.

3.2 Local temperature variations

Temperature variations on active nucleation sites and on inactive areas are shown in Fig. 4, while wall-temperature profiles across the bubble contact diameter during a single nucleation event are presented in Fig. 5. The results are compared for all samples at 300 kW/m^2.

It is evident from the Fig. 4 that the temperature difference between the active nucleation site and the inactive area is the largest on the reference surface (SS). Prior to the nucleation, the wall temperature gradually increases until the nucleation activation temperature (roughly 120 °C) is reached. As the bubble begins to grow, the heat is utilized for the phase change, which causes the local temperature to drop down to around 102 °C. The entire nucleation event repeats itself with the frequency of 30 Hz in this case, even though the average frequency for all nucleation sites is 25 Hz. In the area with no nucleation activity, the wall temperature is much higher and equals to approximately 138 °C. The wall temperature in the inactive region also fluctuates due to the natural convection and nearby nucleations, which cause movement of the liquid water. Temperature profiles across a single nucleation site on the SS sample [e.g. see Fig 5(a)] reveal that the bubble reaches its final contact diameter approximately 5 ms after the beginning of nucleation. Maximum bubble contact diameters are on average 4 mm at 300 kW/m^2, but might also exceed 6 mm in some cases. We observed comparable heat transfer performance between SS and F1 samples [e.g. see Fig. 4(d) and Fig. 5(d)]. The maximum bubble contact diameters were determined to be between 1.3 and 6.3 mm and the average recorded nucleation frequency was around 26 Hz. Temperature differences between the active nucleation sites and the inactive areas are also significant. However, there is one important distinction between the two samples: nucleation activation temperatures were approximately 4 K higher on the sample F1. Boiling curves also revealed that the average temperatures were constantly higher on the F1 sample.

On the samples F2 and F3 [e.g. see Fig. 4(e,f) and Fig. 5(e,f)] the bubble contact diameters were approximately two times smaller compared to the surfaces F1 and SS and the bubble growth time was shorter. However, the bubble contact diameters were the smallest on the surface F4 and ranged between 0.4 mm and 1.8 mm. Bubble nucleation site density was also by far the highest on the surface F4 and reached 200 cm^{-2} at the heat flux of 300 kW/m^2. There was virtually no surface area without boiling activity and the average wall temperatures on an active nucleation site and the inactive area were practically the same.

The highest nucleation frequency of 100 Hz was recorded on the biphilic surface $BPI_{0.25}$. Fig. 5(c) reveals that the bubble growth time was only roughly 2 ms and the maximum contact diameter of a growing bubble was 1 mm. Hydrophobic spots on $BPI_{0.25}$ define the locations of active nucleation sites [12] and nucleation site density was therefore equal to the density of hydrophobic spots, which is 44 cm^{-2}. Certain parts of the superhydrophilic network around the hydrophobic spots never a come into contact with the growing vapor bubbles and this area had consistently higher temperature compared to the active nucleation site as presented in Fig. 4(c).

Fig. 4 reveals that the wall temperatures on the active nucleation sites drop down to about 105 °C or less during each nucleation event. This is true for all surface types except for the SHPI surface, where the wall temperature on a given active nucleation site on average fluctuated between 119 °C and 114 °C. Temperature profiles across the growing vapor bubble on SHPI foil in Fig. 5(b) confirm that the temperature drop during each nucleation had significantly lower amplitude compared to the other surfaces.

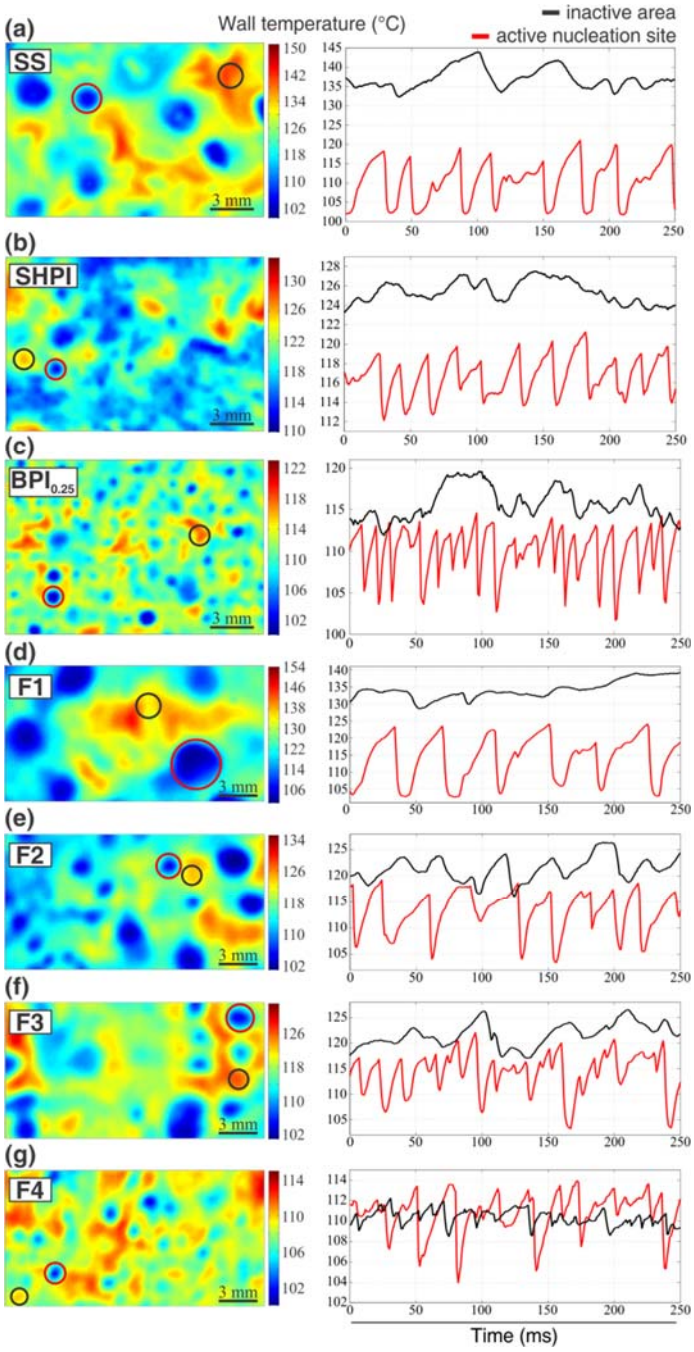

Fig 4: Sample IR images (left) and wall-temperature fluctuations (right) at 300 kW/m^2 on an active nucleation site (in red) and an inactive area (in black). (a) Bare stainless steel, (b-c) PDMS-silica coated samples, and (d-g) non-coated laser textured samples.

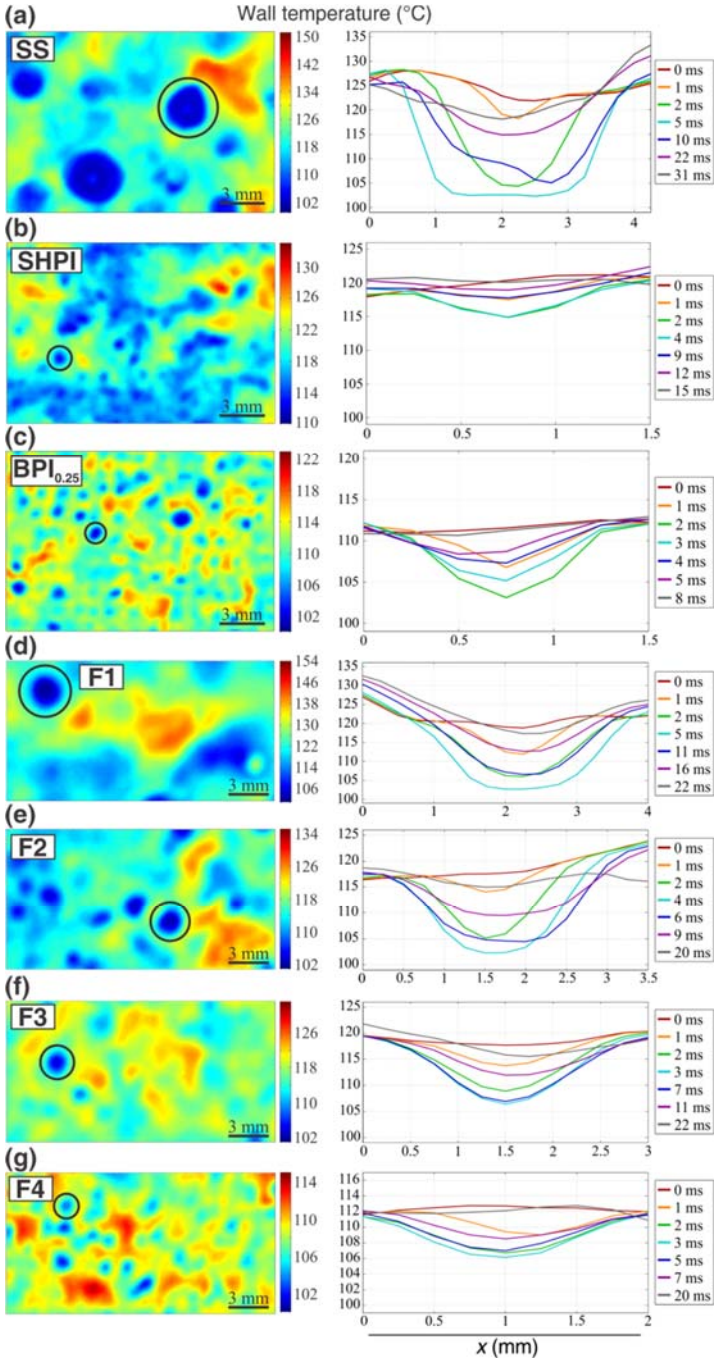

Fig 5: Sample IR images (left) and wall-temperature profiles (right) across the bubble contact diameter during a single nucleation event at 300 kW/m^2. (a) Bare stainless steel, (b-c) PDMS-silica coated samples, and (d-g) non-coated laser textured samples.

3.3 Wall-temperature distributions

On one hand, high-speed IR recordings provide an excellent insight into the boiling phenomena on various engineered surfaces, however a comprehensive analysis is rather time consuming due to the large amount of data. Fig. 4 and Fig. 5 show only the results on a small, localized part of the boiling surface during a relatively short period. Therefore, a constant concern

whether the selected areas and the selected time frames are representative for the entire process is always present. On the other hand, the process of obtaining the boiling curves in Fig. 2(d) is fairly straightforward. However, they show only the average heat flux versus the spatiotemporal averaged wall superheat. To overcome the gap between the transient temperature fields and the boiling curves, we recently proposed a new method of calculating the temperature distributions on the boiling surface on the basis of a series of temperature fields obtained from high-speed IR camera recordings [23]. All the IR temperature readings at a given heat flux during a 10 s recording period (e.g. 10,000 frames) are arranged into equidistant temperature intervals and a probability density function is obtained for each interval. Each probability density is assumed to correspond to the temperature in the middle of the interval in question. The analysis requires a sufficiently long time interval to ensure representative results.

Fig. 6 shows wall-temperature distributions for all surfaces at heat fluxes up to 400 kW/m^2. From Fig. 6(a,d) it is apparent that the surfaces SS and F1 exhibit highest wall-temperature deviations. Maximum local superheats on these two surfaces are in the excess of 20 K at low heat fluxes and close to 60 K at 300 kW/m^2. During boiling on smooth surfaces where large bubbles with large contact diameters are formed, local hot spots start to appear within the bubble contact area as a result of a local dryout [23,24,29]; the temperature of a hot spot can significantly exceed the average wall superheat. By solving a 3-dimensional (3-D) inverse heat conduction problem, we recently showed that the local heat flux and heat transfer coefficient on the location of the hot spot are considerably reduced [29]. Theofanous et al. [24] also proved that the life span and the number of the local hot spots increase with the increasing heat flux and ultimately, the liquid water's access to active nucleation sites is hindered to such extent that it does not rewet one or more of these spots and they further grow in size, which leads to the heater burnout. We can confirm that temperature values on the right-hand side of the wall-temperature distributions correspond to the local temperatures of the hot spots. At the same time, the distributions for the surfaces SS and F1 are bimodal (e.g. at 300 kW/m^2) with the first peak at the superheat of 3 K and the second at 24 K. The temperature of the first peak corresponds to the temperature underneath the vapor bubble after the contact diameter grows to its final size [e.g. see Fig. 5(a,d)]. For the surfaces SS and F1 this temperature is equal to 103 °C. To summarize, large vapor bubbles with the contact diameters of several millimeters produce large areas with a decreased temperature, which reflects in an additional low-temperature peak in the wall-temperature distribution. Furthermore, local hot spots are formed underneath large bubbles and this reflects in an elongated tail on the right side of the distribution.

Despite the fact that the surface F1 underwent modification with the aim of a heat transfer enhancement, the nucleation site density, the nucleation frequency, and the bubble sizes are very similar to those recorded on bare stainless steel (SS foil). Relatively shallow microstructures without any microcavities [see Fig. 2(c)] did not trigger additional bubble nucleations or significantly reduce bubble growth times. However, Fig. 2(d) shows that the average wall superheat was constantly higher on the surface F1 compared to the reference surface SS. Comparison of the temperature fluctuations presented in Fig. 4(a,d) further showes that the nucleation activation temperatures on the surface F1 were 4 K higher compared to the

surface SS. This difference cannot be contributed to the measurement error, since the expanded measurement uncertainty of IR thermography was estimated at 2 K [12]. Differences in the activation temperatures between the surfaces F1 and SS were also observed on all other nucleation sites. Sample F1 was hydrophilic with a contact angle of 64° and the unmodified surface SS exhibited a contact angle of 88°. Surfaces with a higher wettability require higher energy for the nucleation to occur [7,12,30,31], which in turn results in a higher activation temperature. At the same time, the replenishment of the nucleation sites is enhanced on hydrophilic surfaces and the possibility of formation of local dryouts (hotspots) is reduced. This theory is in accordance with our experimental results, since the maximum wall temperatures are lower on the surface F1 compared to the surface SS, in spite of higher activation temperatures on the former.

Similar conclusion can be drawn from the comparison of the wall temperature distributions on the surfaces F2 and F3 [see Fig. 6(e,f)]. Both surfaces had a comparable roughness and microstructure [18], but the surface F2 was hydrophilic with a contact angle of 66° and the surface F3 was superhydrophilic with a contact angle below 1°, which was the limit of our equipment's measurement capability. Analysis of the transient temperature fields proved that the activation temperatures on the surface F3 were constantly higher compared to F2. As a result, the average wall superheat on the surface F3 was more than 1 K higher throughout the entire measurement range of heat fluxes [see Fig. 2(d)]. However, wall-temperature distributions presented in Fig. 6(e) and (f) show that the local maximum temperatures were lower on the surface F3. Our explanation of this is based on the limited bubble growth on the structured superhydrophilic (e.g. super wicking) surface [see Fig. 3(b)] and the stimulated rewetting of the nucleation site after bubble departure. Higher activation temperatures and lower local maximum temperatures result in the shifting of the peak of probability density function to the right, e.g. the skewness (*Sk*) decreases. For example, at 300 kW/m^2 the *Sk* for the sample F2 is 0.33 and for the F3 it equals to -0.66.

Based on the results and discussion provided above, one could claim that the surface F1 should provide lower activation temperatures as F3 due to the higher contact angle of the former surface. Nevertheless, one needs to bear in mind that the surfaces F1 and F3 cannot be *directly* compared only on the basis of their wettability; instead a comparison of boiling behavior on both surfaces should also take into account their *substantial* differences in the surface micro- and nanostructure. On the contrary, surfaces F2 and F3 have similar microstructure (e.g., see Fig. 2(a) and ref. [18] for details about the surface roughness parameters). It was recently published [32] that the intrinsic contact angle as a surface factor is not a sufficient parameter to predict the boiling performance. Therefore, we believe that further systematic research isolating the influence of the wettability and surface micro/nanostructure is needed to independently study effects of surface roughness, wettability, porosity, and other surface factors influencing the nucleate boiling process.

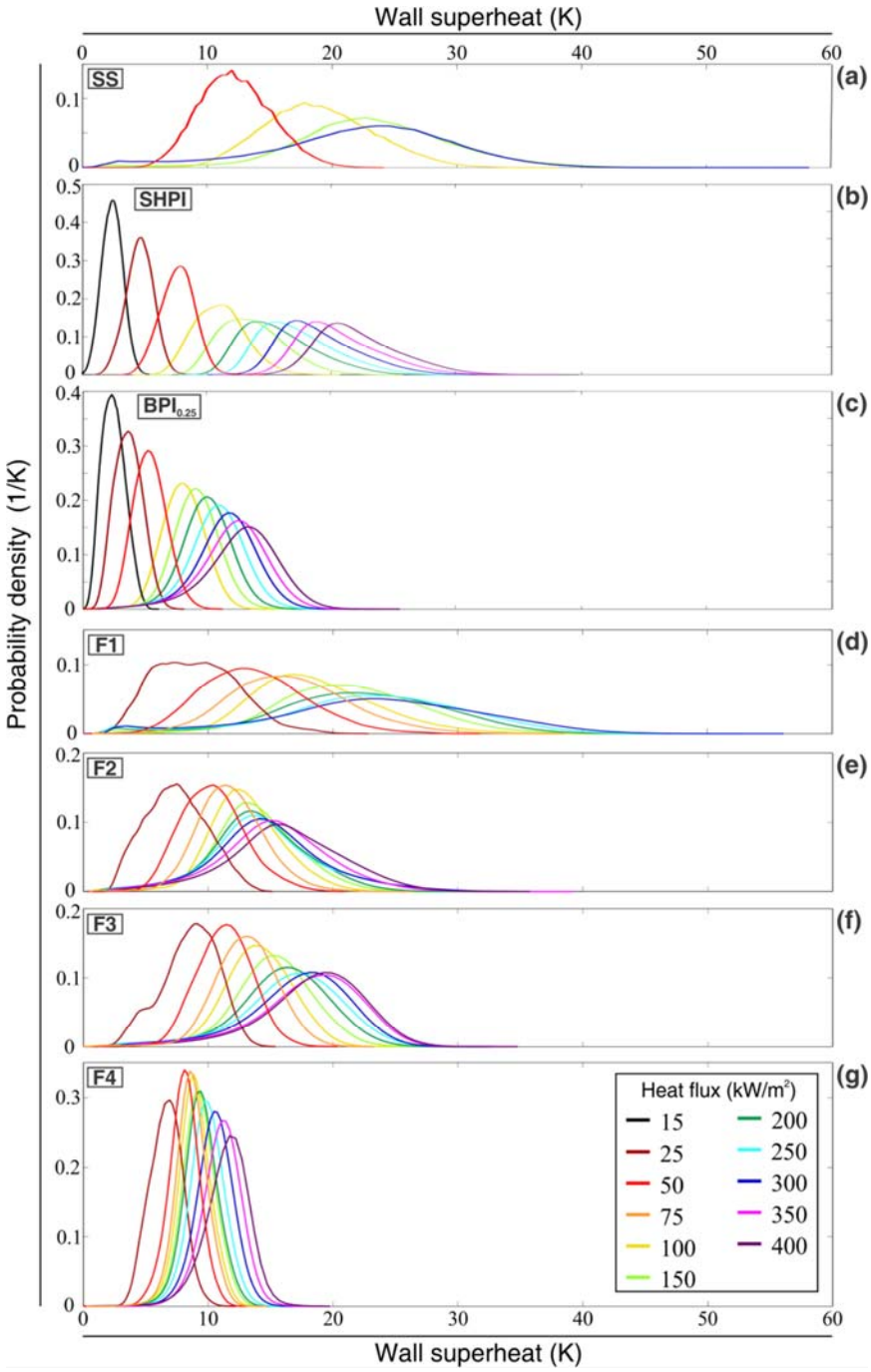

Fig 6: Wall-temperature distributions on (a) bare stainless steel, (b-c) PDMS-silica coated surfaces, and (d-g) non-coated laser textured surfaces.

The nucleation site density on the surface F4 was one order of magnitude higher compared to all the other samples. This was due to the heterogeneous wettability and multi-scale microcavities on the surface [see Fig. 2(c)], which served as potential active nucleation sites in a wide range of wall superheats [18]. Virtually, the entire boiling surface was in contact with the growing vapor bubbles that formed at higher frequencies compared to other laser processed samples F1-F3. Fast emerging bubbles with relatively small contact diameters [see Fig. 4(g)]

prevent the formation of local hot spots. As a result, the wall-temperature distribution for the surface F4 demonstrate the lowest temperature deviation and the shortest tail at higher wall superheats (i.e., the lowest maximum temperatures) among all of the tested samples. The standard deviation of the wall temperature is 1.5 K on the surface F4 at 300 kW/m^2. On the surface BPI$_{0.25}$, it is 3.2 K and on all other surfaces it is in excess of 4 K.

It should be emphasized that the thickness of the heat transfer surfaces in real applications are usually much higher than in our experiments. From practical sense, there is still a need to measure wall-temperature distributions with thicker substrates and compare it with our current results. In future investigations we are aiming to utilize recently proposed fluorescence-based technique [35], which allows submicron transient temperature mapping inside the erbium-doped fluoride glass during the nucleate boiling process. Temperature measurements just underneath the boiling surface and at different thickness levels should reveal the influence of heater thickness on wall-temperature distributions.

The effect of surface coating

Surfaces SS and F1-F4 were all non-coated stainless steel foils, whereas the surfaces SHPI and BPI$_{0.25}$ were produced on steel foil coated with a 1-μm-thick layer of PDMS–silica, as stated in Table 1. More than 97% of the BPI$_{0.25}$ surface was also treated with a nanosecond pulsed laser to produce a superhydrophilic network around the hydrophobic areas. During this process, most of the coating was ablated as explained by Zupančič et al. [12]. Therefore, only the SHPI surface is fully coated with the annealed PDMS-silica coating with the approximate thickness of 1 μm.

The set of experimental results on this surface undoubtedly stands out from the rest. Transient temperature fields in Fig. 4(b) and Fig. 5(b) show that minimum temperatures on the active nucleation sites were significantly higher compared to all of the other tested surfaces. Finally, the wall-temperature distribution in Fig. 6(b) confirms that the minimum wall temperature is constantly increasing with the increasing heat flux and reaches 112 °C at 400 kW/m^2. This trend continues all the way up to the burnout at 1400 kW/m^2 (e.g., see refs. [18] and [23]). On all of the other surfaces, the tails of the distributions at low wall superheats are at or close to the water saturation temperature even at a high heat flux. The final conclusion regarding the coating effect is that the annealed PDMS-silica coating increases the thermal resistance of the entire heater. Moreover, the prolonged thermal response across the coating prevents accurate dynamic measurements of wall temperatures with the technique applied. Heat is generated inside the metal foil, which is coated on the bottom with high emissivity paint and with the PDMS-silica coating on the top. Even though the values on the boiling curve for the SHPI surface are comparable with many results in the present literature [32–34], we can confirm that the IR temperature measurement readings on the bottom of the high-emissivity coating provide values higher the actual wall-temperatures at the surface/fluid interface especially at high heat fluxes.

For both research and application purposes in the development of enhanced heat transfer surfaces, coating-free laser texturing might become the current cutting-edge technology enabling a more accurate analysis compared to coated surfaces.

4 Conclusions

Nucleate boiling performance was evaluated on 25-μm stainless steel foils with the use of double-distilled water as the working fluid. Several surfaces were functionalized either by the application of a PDMS-silica coating, which was potentially followed by a heat treatment; or solely by nanosecond–laser texturing. The recently proposed concept of wall-temperature distributions was utilized in order to emphasize important differences in the boiling process on all of the tested samples. Our results clearly lead to the following conclusions:

- Smooth stainless steel surface requires high nucleation activation temperatures and the bubble departure diameter as well as the bubble contact diameter can exceed 5 mm. Wall-temperature distribution in the nucleate boiling regime is bimodal with the first peak at the superheat of roughly 3 K, which is equal to the superheat underneath the growing bubbles. Distributions also reveal that the maximum local superheat can exceed 50 K as a result of local hotspots.
- Enhanced boiling performance on a PDMS-silica coated biphilic surface and laser textured surfaces results in lower standard deviations and shorter tails of the wall-temperature distributions at higher wall superheats. The highest measured nucleation site density was 200 cm^{-2} at 300 kW/m^2 and it was achieved on a laser textured surface, which was strewn with microcavities and had a heterogeneous wettability. This surface provided the highest heat transfer coefficient among all of the tested surfaces, while the standard deviation of the wall temperature was only 1.5 K at 300 kW/m^2. On all of the other samples, the standard deviation of the temperature distributions exceeded 3 K.
- A textured superhydrophilic surface enhances liquid replenishment on the active nucleation sites and thus prevents the occurrence of distinct local hot spots. It promotes small bubble departure diameters and - at the same time - also requires relatively high nucleation activation temperatures. Higher activation temperatures and lower local maximum temperatures result in the peak shifting of the wall-temperature distribution towards higher wall superheats, e.g., negative skewness (*Sk*) can be observed. We demonstrated that it is possible to clearly differentiate between boiling on a superhydrophilic and a slightly hydrophilic surface solely on the statistical parameters of the wall-temperature probability density function.
- The wall-temperature distributions also revealed that the annealed PDMS-silica coating significantly increases the thermal resistance of the thin-foil heater. As a result, the temperatures at the bottom side of the foil, which are measured with a high-speed IR camera, are higher than the actual temperatures at the solid/fluid interface. In contrast, enhanced heat transfer surfaces produced using the direct laser texturing method are not prone to such measurement errors, since the method does not require any additional coatings. Therefore, nanosecond laser texturing was proved to be a versatile and low-cost method having a high potential to become a future cutting-edge technology in the development of surfaces for enhanced heat transfer for research and real applications.

Acknowledgements

The authors acknowledge the financial support from the state budget by the Slovenian Research Agency (Program Nos. P2-0223 and P2-0392).

References

[1] S. Launay, A.G. Fedorov, Y. Joshi, A. Cao, P.M. Ajayan, Hybrid micro-nano structured thermal interfaces for pool boiling heat transfer enhancement, Microelectronics J. 37 (2006) 1158–1164. doi:10.1016/j.mejo.2005.07.016.

[2] Z. Yao, Y.W. Lu, S.G. Kandlikar, Effects of nanowire height on pool boiling performance of water on silicon chips, Int. J. Therm. Sci. 50 (2011) 2084–2090. doi:10.1016/j.ijthermalsci.2011.06.009.

[3] I.C. Bang, J. Buongiorno, L.-W. Hu, H. Wang, Measurement of Key Pool Boiling Parameters in Nanofluids for Nuclear Applications, J. Power Energy Syst. 2 (2008) 340–351. doi:10.1299/jpes.2.340.

[4] C. Lee, H. Kim, H.S. Ahn, M.H. Kim, J. Kim, Micro/nanostructure evolution of zircaloy surface using anodization technique: Application to nuclear fuel cladding modification, Appl. Surf. Sci. 258 (2012) 8724–8731. doi:10.1016/j.apsusc.2012.05.081.

[5] I. Golobic, a E. Bergles, Effects of heater-side factors on the saturated pool boiling critical heat flux, Exp. Therm. Fluid Sci. 15 (1997) 43–51. doi:10.1016/S0894-1777(96)00170-7.

[6] I.L. Pioro, W. Rohsenow, S.S. Doerffer, Nucleate pool-boiling heat transfer. I: Review of parametric effects of boiling surface, Int. J. Heat Mass Transf. 47 (2004) 5033–5044. doi:10.1016/j.ijheatmasstransfer.2004.06.019.

[7] Y. Takata, S. Hidaka, T. Uraguchi, Boiling Feature on a Super Water-Repellent Surface, in: Proc. Fifth Int. Conf. Enhanc. Compact Ultra-Compact Heat Exch. Sci. Eng. Technol., 2005: pp. 300–304. doi:10.1080/01457630600793962.

[8] S.J. Kim, I.C. Bang, J. Buongiorno, L.W. Hu, Surface wettability change during pool boiling of nanofluids and its effect on critical heat flux, Int. J. Heat Mass Transf. 50 (2007) 4105–4116. doi:10.1016/j.ijheatmasstransfer.2007.02.002.

[9] Y.-W. Lu, S.G. Kandlikar, Nanoscale Surface Modification Techniques for Pool Boiling EnhancementA Critical Review and Future Directions, Heat Transf. Eng. 32 (2011) 827–842. doi:10.1080/01457632.2011.548267.

[10] D.E. Kim, D.I. Yu, D.W. Jerng, M.H. Kim, H.S. Ahn, Review of boiling heat transfer enhancement on micro/nanostructured surfaces, Exp. Therm. Fluid Sci. 66 (2015) 173–196. doi:10.1016/j.expthermflusci.2015.03.023.

[11] D. Attinger, C. Frankiewicz, A.R. Betz, T.M. Schutzius, R. Ganguly, A. Das, C.-J. Kim, C.M. Megaridis, Surface engineering for phase change heat transfer: A review, MRS Energy Sustain. 1 (2014) E4. doi:10.1557/mre.2014.9.

[12] M. Zupančič, M. Steinbücher, P. Gregorčič, I. Golobič, Enhanced pool-boiling heat transfer on laser-made hydrophobic/superhydrophilic polydimethylsiloxane-silica patterned surfaces, Appl. Therm. Eng. 91 (2015) 288–297. doi:10.1016/j.applthermaleng.2015.08.026.

[13] A.Y. Vorobyev, C. Guo, Multifunctional surfaces produced by femtosecond laser pulses, J. Appl. Phys. 117 (2015) 33103. doi:10.1063/1.4905616.

[14] A.M. Kietzig, S.G. Hatzikiriakos, P. Englezos, Patterned superhydrophobic metallic surfaces, Langmuir. 25 (2009) 4821–4827. doi:10.1021/la8037582.

[15] D. V. Ta, A. Dunn, T.J. Wasley, R.W. Kay, J. Stringer, P.J. Smith, C. Connaughton, J.D. Shephard, Appl. Surf. Sci. 357 (2015) 248–254. doi:10.1016/j.apsusc.2015.09.027.

[16] V.D. Ta, A. Dunn, T.J. Wasley, J. Li, R.W. Kay, J. Stringer, P.J. Smith, E. Esenturk, C. Connaughton, J.D. Shephard, Laser textured superhydrophobic surfaces and their applications for homogeneous spot deposition, Appl. Surf. Sci. 365 (2016) 153–159. doi:10.1016/j.apsusc.2016.01.019.

[17] C.M. Kruse, T. Anderson, C. Wilson, C. Zuhlke, D. Alexander, G. Gogos, S. Ndao, Enhanced pool-boiling heat transfer and critical heat flux on femtosecond laser processed stainless steel surfaces, Int. J. Heat Mass Transf. 82 (2015) 109–116. doi:10.1016/j.ijheatmasstransfer.2014.11.023.

[18] M. Zupančič, M. Može, P. Gregorčič, I. Golobič, Nanosecond laser texturing of metal surfaces with non-uniform wettability for enhanced boiling heat transfer, Appl. Surf. Sci. (2017). doi:10.1016/j.apsusc.2016.12.120.

[19] S. Nukiyama, The maximum and minimum values of the heat Q transmitted from metal to boiling water under atmospheric pressure, Int. J. Heat Mass Transf. 9 (1966) 1419–1433. doi:10.1016/0017-9310(66)90138-4.

[20] T.G. Theofanous, J.P. Tu, A.T. Dinh, T.N. Dinh, The boiling crisis phenomenon part I: Nucleation and nucleate boiling heat transfer, Exp. Therm. Fluid Sci. 26 (2002) 775–792. doi:10.1016/S0894-1777(02)00192-9.

[21] I. Golobic, J. Petkovsek, D.B.R. Kenning, Bubble growth and horizontal coalescence in saturated pool boiling on a titanium foil, investigated by high-speed IR thermography, Int. J. Heat Mass Transf. 55 (2012) 1385–1402. doi:10.1016/j.ijheatmasstransfer.2011.08.021.

[22] I. Golobič, E. Pavlovič, J. Von Hardenberg, M. Berry, R.A. Nelson, D.B.R. Kenning, L.A. Smith, Comparison of a Mechanistic Model for Nucleate Boiling with Experimental Spatio-Temporal Data, Chem. Eng. Res. Des. 82 (2004) 435–444. doi:http://dx.doi.org/10.1205/026387604323050146.

[23] I. Golobič, M. Zupančič, Wall-temperature distributions of nucleate pool boiling surfaces vs. boiling curves: A new approach, Int. J. Heat Mass Transf. 99 (2016) 541–547. doi:10.1016/j.ijheatmasstransfer.2016.04.033.

[24] T.G. Theofanous, T.N. Dinh, J.P. Tu, A.T. Dinh, The boiling crisis phenomenon part II: Dryout dynamics and burnout, Exp. Therm. Fluid Sci. 26 (2002) 793–810. doi:10.1016/S0894-1777(02)00193-0.

[25] B.S. Kim, S. Shin, D. Lee, G. Choi, H. Lee, K.M. Kim, H.H. Cho, Stable and uniform heat dissipation by nucleate-catalytic nanowires for boiling heat transfer, Int. J. Heat Mass Transf. 70 (2014) 23–32. doi:10.1016/j.ijheatmasstransfer.2013.10.061.

[26] A.R. Betz, J. Xu, H. Qiu, D. Attinger, Do surfaces with mixed hydrophilic and hydrophobic areas enhance pool boiling?, Appl. Phys. Lett. 97 (2010) 13–16. doi:10.1063/1.3485057.

[27] A.R. Betz, J. Jenkins, C.J. Kim, D. Attinger, Boiling heat transfer on superhydrophilic, superhydrophobic, and superbiphilic surfaces, Int. J. Heat Mass Transf. 57 (2013) 733–741. doi:10.1016/j.ijheatmasstransfer.2012.10.080.

[28] N. Zuber, On the stability of boiling heat transfer, Trans. Am. Soc. Mech. Eng. Vol: 80 (1958) 711–720.

[29] J. Petkovsek, Y. Heng, M. Zupancic, H. Gjerkes, F. Cimerman, I. Golobic, IR thermographic investigation of nucleate pool boiling at high heat flux, Int. J. Refrig. 61 (2016) 127–139. doi:10.1016/j.ijrefrig.2015.10.018.

[30] B. Bourdon, R. Rioboo, M. Marengo, E. Gosselin, J. De Coninck, Influence of the Wettability on the Boiling Onset, Langmuir. 28 (2012) 1618–1624. doi:10.1021/la203636a.

[31] D. Turnbull, Kinetics of heterogeneous nucleation, J. Chem. Phys. 18 (1950) 198–203. doi:doi:10.1063/1.1747588.

[32] M.M. Rahman, E. Ölçeroğlu, M. McCarthy, Role of wickability on the critical heat flux of structured superhydrophilic surfaces, Langmuir. 30 (2014) 11225–11234. doi:10.1021/la5030923.

[33] M.M. Rahman, E. Ölçeroğlu, M. McCarthy, Scalable Nanomanufacturing of Virus-templated Coatings for Enhanced Boiling, Adv. Mater. Interfaces. 1 (2014) 1–6. doi:10.1002/admi.201300107.

[34] H. Jo, S. Kim, H.S. Park, M.H. Kim, Critical heat flux and nucleate boiling on several heterogeneous wetting surfaces: Controlled hydrophobic patterns on a hydrophilic substrate, Int. J. Multiph. Flow. 62 (2014) 101–109. doi:10.1016/j.ijmultiphaseflow.2014.02.006.

[35] I. Sedmak, I. Urbančič, R. Podlipec, J. Štrancar, M. Mortier, I. Golobič, Submicron thermal imaging of a nucleate boiling process using fluorescence microscopy, Energy, 109 (2016) 436-445. doi:10.1016/j.energy.2016.04.121.

List of figures

List of tables